Biomedicine & Pharmacotherapy 188 (2025) 118208

Contents lists available at ScienceDirect

Biomedicine & Pharmacotherapy

journal homepage: www.elsevier.com/locate/biopha

From lichen to organoids: Usnic acid enantiomers show promise against Cholangiocarcinoma via MNK2 targeting and MAPK pathway modulation

Valeria Cavalloro [a,b], Alessio Malacrida [c], Mariarosaria Miloso [c], Davide Ronchi [d], Alessio Porta [e], Alice Fossati [a,b], Gabriele Gheza [f], Silvia De Siervi [g], Stefania Mantovani [h], Barbara Oliviero [h], Mario Umberto Mondelli [h], Luisa Pugliese [i], Cristian Turato [g,*], Emanuela Martino [a,b,**], Simona Collina [j]

[a] Department of Earth and Environmental Sciences, University of Pavia Via Ferrata 1, Pavia 27100, Italy
[b] NBFC—National Biodiversity Future Center, Piazza Marina 61, Palermo 90133, Italy
[c] School of Medicine and Surgery, University of Milan-Bicocca, Monza 20900, Italy
[d] Department of Electrical, Computer and Biomedical Engineering, Via A. Ferrata, 5, Pavia 27100, Italy
[e] Department of Chemistry, University of Pavia, Via Taramelli, 12, Pavia 27100, Italy
[f] BIOME Lab, Department of Biological, Geological and Environmental Sciences, Alma Mater Studiorum - University of Bologna, Bologna 40126, Italy
[g] Department of Molecular Medicine, University of Pavia, Via Forlanini 6, Pavia 27100, Italy
[h] Research Department, Laboratory of Clinical Immunology, Fondazione IRCCS Policlinico San Matteo, Pavia 27100, Italy
[i] S.A.F.AN. BIOINFORMATICS s.a.s., via Don Giovanni Grioli 4, Torino 10137, Italy
[j] Department of Drug Sciences, University of Pavia, Via Taramelli, 12, Pavia 27100, Italy

ARTICLE INFO

Keywords:
Rare Cancer
Usnic acid enantiomers
Cladonia foliacea
Organoids
Cholangiocarcinoma
MAPK pathway

ABSTRACT

Cholangiocarcinoma (CC) remains one of the most challenging biliary tract malignancies, with limited therapeutic options and poor survival rates. We report the discovery and mechanistic investigation of usnic acid (UA) enantiomers as novel anti-CC agents. We identified the lichen *Cladonia foliacea* as a potential source of anticancer agents and developed a sustainable protocol to isolate (*S*)-UA as the most abundant metabolite. Our comprehensive comparative study of both enantiomers revealed time-dependent enantio-preference in their anti-cancer activity. While (*S*)-UA demonstrated twice the potency at 24 h, (*R*)-UA exhibited nearly ten-fold greater activity at 48 h and 72 h, particularly at lower concentrations (2.9 and 29 mM). Overall, both enantiomers inhibited EGI-1 cell proliferation in the micromolar range in a dose- and time-dependent manner. In silico studies and kinase profiling identified MNK2 as a primary target, with subsequent validation confirming direct binding and inhibition. Mechanistic studies demonstrated that UA enantiomers modulate the MAPK pathway, leading to decreased phosphorylation of eIF4E and suppression of cancer-promoting proteins. The successful translation of activity from 2D cell cultures to patient-derived 3D organoid models further validates their therapeutic potential. Our findings establish usnic acid as a promising natural product scaffold for CC treatment and provide detailed insights into its mechanism of action through MNK2 targeting and MAPK pathway modulation, with important considerations for enantiomer-specific temporal efficacy.

1. Introduction

Cancer is the second leading cause of death worldwide. However, new therapeutic options have been developed, and mortality from some types of cancer has drastically decreased. This positive trend is due to the discovery of new effective treatments and the increased awareness among the population of the importance of screening [1]. Unfortunately, this positive trend cannot be generalized to all cancer types, as in the case of rare tumors. Among these, cholangiocarcinoma (CC), a biliary tract cancer, stands out as particularly aggressive, representing almost 5 % of all gastrointestinal cancers [2]. Its incidence varies significantly by geographic region, ranging from 2 cases per 100, 000 people in most high-income countries to rates up to 40-fold higher in some Asian regions [3,4]. Despite its relatively low incidence in

* Corresponding author.
** Corresponding author at: Department of Earth and Environmental Sciences, University of Pavia, Via Ferrata 1, Pavia 27100, Italy.
E-mail addresses: cristian.turato@unipv.it (C. Turato), emanuela.martino@unipv.it (E. Martino).

https://doi.org/10.1016/j.biopha.2025.118208
Received 4 April 2025; Received in revised form 12 May 2025; Accepted 21 May 2025
Available online 23 May 2025

Western countries, CC is associated with an extremely high mortality rate, with 95 % of patients dying within five years. This poor prognosis derives primarily from two factors: the difficulty in detecting early biliary lesions due to the complicated branches of the biliary tree, the fact that often CC emerges in the setting of a normal liver, and the limited availability of effective treatments or drugs [5–7]. In recent years, the discovery of new anti-CC agents has been facilitated by the development of 3D models, namely organoids. The first tissue-derived organoid was described in 2009 and was an intestinal organoid [8]. This technique has been more and more defined, and it is now gaining a footprint in the study of the physiopathology of selected organs. Particularly, CC organoids have been recently exploited for the classification of subtypes, modeling their metastatic behavior, and testing new active ingredients [9–11].

Numerous research teams are working to discover and develop new treatments against cholangiocarcinoma. These approaches include photodynamic therapy, photoimmunotherapy, antibody-drug conjugates, and small molecules, both synthetic and derived from natural sources [5]. Among these strategies, nature-aided drug discovery (NADD) has emerged as particularly promising, as nature provides an almost limitless source of molecules with anti-cancer potential [12].

Many NADD campaigns have been conducted on innovative biomasses, such as marine organisms and lichens, obtaining positive results to counteract different human diseases. Among natural sources, lichens have emerged as promising candidates for anti-cancer drug discovery. These unique organisms are symbiotic associations between a fungus (mycobiont), a green alga or a cyanobacterium (photobiont), and several other microorganisms [13]; the photobiont produces nourishment, while the mycobiont protects from drying and solar radiation [14]. This partnership allows the lichen to survive even in difficult environmental conditions and to colonize different substrates, both natural, as rocks, wood, soil, mosses, and other lichens, and artificial, as cement, glass, and plastics [15]. The greatest success of lichens has been demonstrated in the anti-cancer and anti-microbial fields, mainly due to the characteristics of their secondary metabolites, whose structures are often absent in other natural matrices.

While lichen metabolites have shown great potential in cancer treatment, few data are available for their application to rare cancers like CC. Our work addresses this gap by investigating *Cladonia foliacea* (Huds.) Willd., a lichen species that is widespread in Northern Italy and easy to collect, which are fundamental characteristics of a biomass in the NADD process. This species is particularly valuable as a source of (*S*)-Usnic acid [(S)-UA], a dibenzofuran class metabolite that, unlike its well-studied (*R*)-enantiomer, remains largely unexplored despite its potential therapeutic value [16], mainly because of its lower occurrence in nature [17]. Recent literature highlighted the potential of UA to target multiple hallmarks of cancer, such as inhibiting abnormal growth signals, inducing cell death, disrupting metabolism, preventing angiogenesis, reducing cell migration and invasion, modulating immune response, and exhibiting anti-inflammatory properties. Although its antiproliferative effects in vitro are well documented, further research is needed to evaluate its specific effects on cancer as CC [18–20].

To evaluate the potential of these compounds against CC, we have developed a comprehensive approach combining multiple research methods. Recent advances in 3D cell culture technology, particularly organoids, have provided new opportunities for drug testing. Leveraging these advances, our study begins with the development of a green, scalable method for obtaining (S)-Usnic acid, followed by in silico studies, 2D cell line activity evaluation, and culminating in investigations using 3D organoid cultures.

2. Material and method

2.1. General

All reagents and solvents were obtained by Merck (Italy), Carlo Erba and Panreac. Unless otherwise specified, the commercially available reagents were used as received from the supplier. (+)-Usnic acid was purchased by Carbosynth Ltd.(Compton Berkshire, UK).

Solvent removal has been done with a rotary evaporator (Heidolph Laborota 4000 efficient), compounds weighed with a precision balance (Gibertini E42-B), solid dissolution with ultrasounds (Elma Transsonic T420), while centrifugation has been performed with ALC Centrifugette 4206 (ALC International Srl.) centrifuge.

Microwave assisted solvent extractions (MASE) have been performed exploiting a multimode microwave apparatus (MARSX press, CEM Corporation, Matthews, NC, USA).

The chromatographic analysis was performed with a UHPLC apparatuts JASCO (Lecco, Italy) X-LC system coupled with a MS spectrometer Thermo Scientific (Milan, Italy) LTQ XL HESI-MS/MS system. The column used for chromatographic separation was a Restek Raptor ARC-18 (1.8 μm, 100 ×2.1 mm). equipped with a similar pre-column.Optical rotation values were measured on a Jasco photoelectric polarimeter DIP 1000 using a 0.5 dm cell and a sodium lamp (λ=589 nm)

Proton nuclear magnetic resonance (NMR) spectra were recorded on a Bruker Avance 400 spectrometer operating at 400.13 MHz or JEOL JNM-LA 300 at 300 MHz. Chemical shifts (δ) are reported in parts per million with the solvent reference relative to tetramethylsilane (TMS) internal standard.

2.2. Lichen material

Thalli of *C. foliacea* were sampled from Italy, Lombardia, Province of Pavia, Gamboló, Bosco della Ghisolfa, 45°16'40"N 8°56'05"E, 75 m a.s.l., 12/06/2019, leg. et det. G. Gheza. A voucher specimen was deposited in the herbarium unit of the Earth and Environmental Science Department.

Lichen material was dried in a dry and temperate place until constant weight and next was reduced to a homogenous powder by grounding it with a blade-mill (A10 IKA-Werke GmbH & Co. Staufen, Germany) just before performing the extractions.

2.3. Extraction and UHPLC analysis

10 g of *C. foliacea* were extracted with 200 mL of EtOH or AcOEt. The extraction was carried out under the following experimental conditions: 400 Watts; 80°C; 120 PSI; ramp time 2 min; holding time: 5 minutes; 2 cycles with solvent renewal. Each extract was solubilized at 1 mg/mL and analyzed using a Restek Raptor column (2.1 mm × 100 mm, 1.8 mm) equipped with a pre-column.

After an equilibration period of 5 min, 1 mL of each sample were injected in the UHPLC system. Gradient elution was performed with acetonitrile/water–0.2 %HCOOH (from 10:90–100:0 in 10 min) as a mobile phase, the flow rate was 0.3 mL min^{-1}. The column temperature was maintained at 35 °C with "on-line" oven equipement, and the total run time was 15 min (including a 3 min of column washing performed with pure ACN at same flow).

In order to obtain the best performance of MS specrometer the output flow was split (70/30, 70 % of flow in waste and 30 % of flow, 70 μL min^{-1}, were introduced into MS source).

HESI determinations were performed with MS spectrometer Thermo Scientific (Milan, Italy) LTQ XL HESI-MS/MS system using UHPLC-Flow injection of purified fractions.

HESI Probe: Gas=N2, T = 95°C, Voltage= 3.5 kV; Capillary T = 275°C, Voltage= 46 V, Tube Lens= 71 V. Tune Settings: Multipole 00 Offset = 2.5 V, Lens 0 = - 4.27 V, Multipole 0 Offset =

-5.19 V, Lens 1 = - 8.93, Gate Lens = - 65.3 V, Multipole 1 Offset = - 6.4 V, Multipole RF Amplitude (p-p)= 400 V, Front Lens = - 6.2 V.

Settings for MS-MS and MS^3: detection by CID (Collision Induced Dissociation); Isolation Width: ± 2 d; Activation Q: 0.250; Activation Time 30.0 msec. Isolation width for quantitation ± 2.5 d.

2.4. Isolation of (S)-UA

10 g of *C. foliacea* were extracted with EtOH as previously reported [21].

The raw extract was solubilized in the minimum amount of methanol and left at 4°C overnight. Next, the solid was centrifugated and a mixture of 1 chloroform: 2 ethanol added. Crystallization was promoted by refrigeration. The precipitate was isolated by vacuum filtration with Buchner funnel, washed with cold ethanol and dried in air. 74 mg of pure compound were isolated, with a product yield of 0.74 % (expressed as mg of pure metabolite per 100 mg of dry biomass).

The crystals obtained in this way were characterized via NMR, MS and chiroptical analysis and results were coherent with literature [22]:

Molecular formula: $C_{18}H_{16}O_7$; mp 204 °C, *m/z* 344, $[\alpha]_D^{25} = -476^\circ$, **^{1}H NMR** in CDCl3, (ppm): 18.86 (s, 1 H, O**H**), 13.33 (s, 1 H, O**H**), 11.05 (s, 1 H, O**H**), 6.00 (s, 1 H, OCC**H**), 2.70 (s, 3 H, COC**H$_3$**), 2.68 (s, 3 H, COC**H$_3$**), 2.13 (s, 3 H, CCC**H$_3$**), 1.78 (s, 3 H, COCC**H$_3$**). Full characterization is reported in SM.

2.5. In silico investigation

Different computational approaches were followed to identify known targets of *(S)-UA*, study their interaction with the selected compound and furthermore study the interactions among them.

2.5.1. CTI and PPI networks construction

To start, a Compound Target Interaction network was generated via STITCH database (http://stitch.embl.de/ 'Search Tool for Interacting Chemicals'). To construct the network the following parameters of research were applied: text mining, experiments, databases, co-expression, neighborhood, gene fusion, co-occurrence, predictions, medium confidence of interaction score > 0.4 and the research in general was limited to the specie "*Homo sapiens*". The top 10 interactors derived from the research were then pasted inside the STRING database (https://string-db.org "Search Tool for the Retrieval of Interacting Genes/Proteins") to study their interaction and to construct the Protein Protein Interaction network. The same parameters of research used for STITCH were applied to STRING as well. All ten interactors were linked by the PPI network as well, showing their ability to interact with each other and with the selected compound at the same time.

2.5.2. Functional enrichment analysis

The CTI and the PPI network were exported on Cytoscape (https://cytoscape.org/) and merged. The merged network was subjected to the CytoHubba Plugin to rank the interactions among the nodes of the network: CASP3 and MAPK3 were ranked as 1, being the fulcrum of the cluster, followed by RPS6KBP1 (rank 3), MAPK1 (rank 4), SQSTM1 (rank 5), EIF4EBP1 (rank 6), CASP7 (rank7), XBP1 (rank 8), CASP4 (rank 9) and PDK1 (rank 10).

Later, to identify pathological genes among the ten selected, a brief functional enrichment analysis was performed on NDEX Plugin. A civic public database of gene-disease associations was loaded, combining the information contained inside this database and cross-checking it with scientific literature, two of the ten selected genes were identified as responsible for cancer development: MAPK1 and EIF4EBP1.

2.6. MTT assay

Human cholangiocarcinoma EGI-1 cells (DSMZ-German Collection of Microorganisms and Cell Cultures - ACC 385) were cultured in RPMI 1640 medium (Euroclone, Pero, Italy) with 10 % FBS, 1 % L-glutamine, and 1 % Penicillin and Streptomycin. Cells were incubated at 37°C and 5 % CO2 in a humidified incubator.

EGI-1 cells were seeded in 96-well plates at 10,000 cells/well density and were treated with different concentrations of the extracts or pure compounds for 24, 48, and 72 h at 37°C. The culture medium was then replaced with a 3-(4,5-dimethylthiazol-2-ys)-2,5-diphenyltetrazolium bromide (MTT) (Sigma-Aldrich, St Louis, MO) 0.5 mg/mL medium solution. After 2 h of incubation at 37°C, formazan crystals were solubilized in 100 % EtOH and absorbance was read at 560 nm in a microplate reader (BMG Labtech, Germany). Survival cells were calculated normalizing the data to absorbance of non-treated cells.

2.7. Western blotting

EGI-1 cells were seeded in 6-well plates at 250,000 cells/well density and were treated with different concentrations of pure compounds for 30 minutes, 1, 4, 24, and 482 h at 37°C. Cells were lysed using RIPA buffer prepared as follows: 25 mM Tris HCl pH 7.6, 150 mM NaCl, 1 % sodium deoxycholate, 1 % NP-40, 0.1 % SDS, 4 mM PMSF, 1 % aprotinin, 20 mM sodium pyrophosphate, 10 mM sodium. Next, they were subjected to sonication. The protein concentration was determined using the Bradford assay. Subsequently, 10 μg of proteins were separated by SDS-PAGE and transferred onto a nitrocellulose membrane. Western blot analysis was performed according to the manufacturer's instructions for each antibody. The following primary antibodies were used: anti-total ERK 1/2 (1:1000, Cell Signaling), anti P-ERK 1/2 (1:1000, Cell Signaling), and anti-vinculin (1:1000, Santa Cruz). The following secondary antibodies were used: anti mouse, Cy3 conjugate (1:2500, Amersham), anti-rabbit, Cy5 conjugate (1:2500, Amersham) and anti-mouse, HRP conjugate (1:2000). Western blot images were acquired using an Amersham Imagequant 800, with fluorescence detection (for total ERK 1/2 and P-ERK 1/2) and chemiluminescence detection (for Vinculin). ImageJ software was used to quantify protein bands.

2.8. Organoid development

For organoid development, surgically resected intrahepatic cholangiocarcinoma (iCCA) specimens were obtained from two treatment-naïve patients at Fondazione IRCCS Policlinico San Matteo, Pavia, Italy. Tissue samples were stored in tissue storage solution (Miltenyi Biotec) and processed within 24 hours. A written informed consent was obtained from each individual. The study protocol is compliant with the ethical guidelines of the 1975 Declaration of Helsinki and was approved by our institutional ethical committee. Briefly, tissue samples were treated by enzymatic and mechanical dissociation with the human Tumor Dissociation Kit and gentleMACS Dissociator, according to the manufacturer's instructions (Miltenyi Biotec). The cell suspension was filtered in a 70 μm cell strainer and centrifuged twice at 50 g for 2 min and small-cell clusters were then treated in 1 mL of ACK lysing solution (GIBCO) to remove blood cells. Subsequently, cells were resuspended in R&D Systems' Cultrex UltiMatrix Reduced Growth Factor (RGF) Basement Membrane Extract (BME), seeded in low adhesion 24-well plates (GreinerBio), and after polymerization covered with expansion medium. The expansion medium was adapted from the protocol of Nuciforo et al. (PMID: 30067989) and composed of Advanced DMEM/F-12 (GIBCO) with 1 % penicillin/streptomycin (GIBCO), 1 % Glutamax (GIBCO), 10 mM HEPES (GIBCO) with the addition of B-27 (1:50) (GIBCO), N-2 (1:100) (GIBCO), 10 mM nicotinamide (Sigma-Aldrich), 1.25 mM N-acetyl-L-cysteine (Sigma-Aldrich), 10 μM forskolin (Tocris), 10 μM ROCK inhibitor (Y-27632) (Tocris), 5 μM A83–01 (Sigma-Aldrich), 10 nM [Leu15]-gastrin I (Sigma-Aldrich), 50 ng/mL epidermal growth factor (EGF) (R&D Systems), 25 ng/mL hepatocyte growth factor (HGF) (Homemade), 10 % R-Spondin1 conditioned medium (Sigma-Aldrich) and 30 % Wnt3a conditioned medium with Noggin (Sigma-Aldrich).

Organoids were passed by mechanical dissociation and incubation in Cultrex Organoid Harvesting Solution (R&D Systems) for 1 h on ice, every 7–10 days. Following their dissociation and resuspension in Recovery Cell Culture Freezing Medium (GIBCO), the organoids were cryopreserved for freezing.

2.9. Organoid immunofluorescence staining

To perform an immunofluorescence characterization, organoids were fixed in cold 4 % paraformaldehyde (Sigma-Aldrich) for 40 minutes at 4°C and subsequently resuspended in PBS with 0.1 % Tween20 (Applichem) for 10 minutes at 4°C for the permeabilization phase. To reduce background non-specific staining, organoids were blocked in PBS with 0.1 % Triton X-100 (Sigma-Aldrich) and 2 % Bovine Serum Albumin (Pan Biotech) solution, for 1 h at room temperature, and then primary antibodies Epithelial Cell Adhesion Molecule (EpCaM, 1:250; # 53–8326–42, Invitrogen) and cytokeratin 7 (CK7, 1:250; #NBP2–44814, Novus Biologicals) were incubated overnight at 4°C. Fluorochrome-labeled secondary antibodies (1:500; #A-21235, Invitrogen) in PBS solution with the addition of 0.1 % Triton X-100 and 0.5 % BSA, incubated for 1 h at room temperature were used. Nuclei were counterstained with Hoechst33342 (Invitrogen). Confocal images were captured on a Leica SP8 inverted confocal microscope (Leica).

2.10. Organoid treatment

Following 3 days after passaging, to allow the reorganization of split organoids, two different dosages of (S)-UA and (R)-UA (4 μM and 40 μM) were applied, and after 72 h an ATP-based cytotoxicity assay CellTiter-Glo 3D Cell Viability Assay was used to evaluate cell viability according to the manufacturer's instructions (Promega). Luminescence was measured on Polarstar-Omega microplate reader (BMG LABTECH) and results were normalized to vehicle (100 % DMSO). Moreover, during treatment the morphological characteristics of iCCA organoids were monitored throughout time with brightfield images using optical microscopy.

2.11. Statistical Analysis

Data are reported as mean ± standard deviation (SD) from at least three independent experiments. Statistical analysis was performed using GraphPad Prism 3 software (Boston, MA). The differences between control and treated cells were evaluated using one way analysis of variance (ANOVA) followed by Dunnet's multiple comparison test. Statistical significance was set at $p < 0.05$.

3. Results

3.1. Extraction, chemical and biological analysis of C. foliacea crude extract

We subjected *C. foliacea* samples to microwave-assisted solvent extraction (MASE) using two solvents of different polarities: ethanol (6.73 % yield) and ethyl acetate (2.50 % yield). The use of solvents with different polarities and microwave absorbance was strategically chosen to obtain comprehensive coverage of the metabolite profile of lichen.

Next, we performed chemical characterization of crude extracts by UHPLC-HESI-MS/MS analysis, applying an optimized method suitable

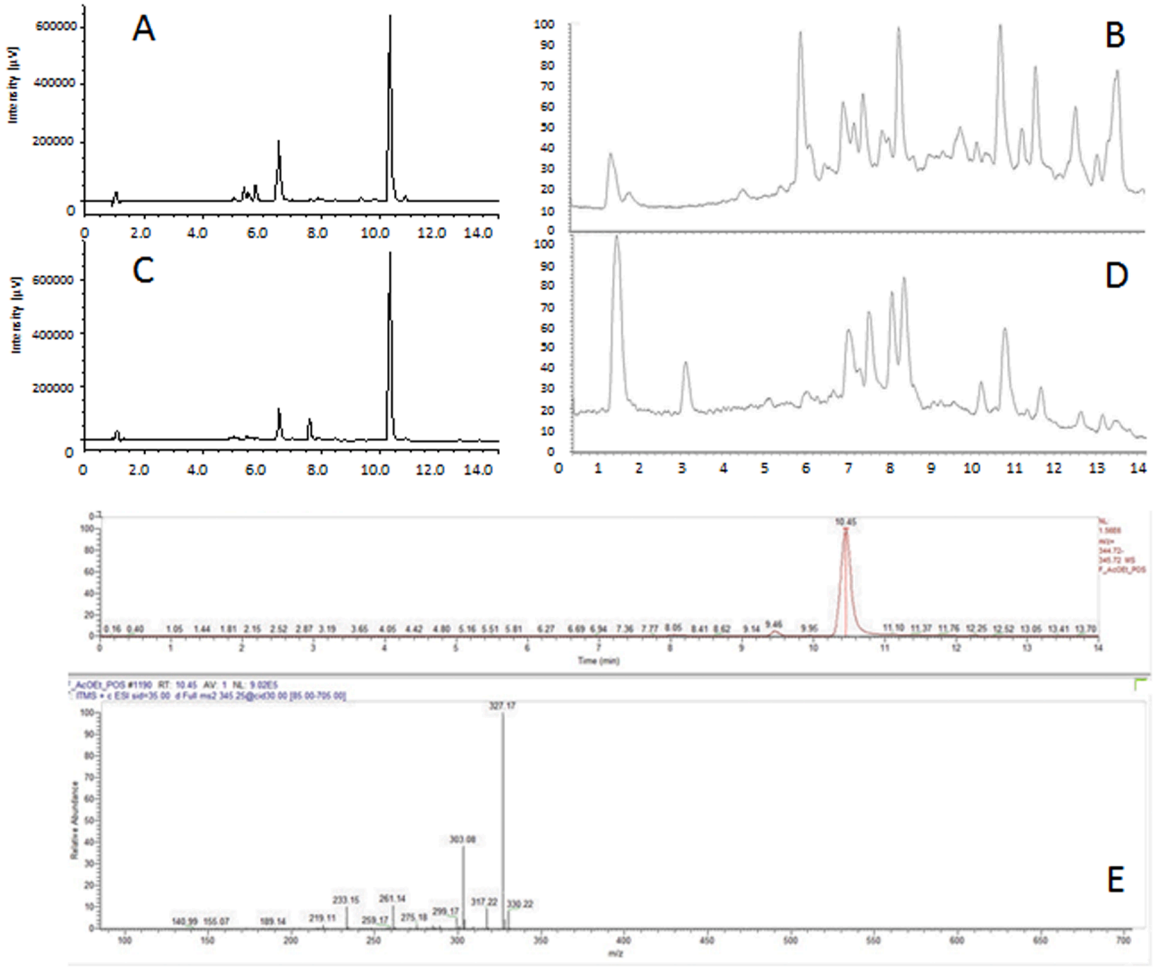

Fig. 1. Panel A: UHPLC-PDA profile of AcOEt extract (λ=280 nm); Panel B: UHPLC ESI profile of AcOEt extract; Panel C: UHPLC-PDA profile of EtOH extract (λ=280 nm); Panel D: UHPLC ESI profile of EtOH extract; Panel E: fragmentation of UA peak (up: SIM chromatogram extracted at 345 *m/z*; down: fragmentation spectrum).

for both extracts. Chromatographi runs were performed using negative and positive modes for ion detection; the MS (TIC) trace in "full scan" mode is reported in Fig. 1. The analysis revealed (*S*)-UA as the principal component (t_R=10.4 min), along with other bioactive metabolites. Notable secondary metabolites, including fumarprotocetraric acid (t_R=6.6 min) and atranorin (t_R=9.8 min) were identified in accordance with our previous publication. Moreover, through its characteristic MS spectra, rangiformic acid was also identified in this species for the first time (t_R=11.3 min; $[M-H]^-$ measured 585.48 *m/z*, main fragment 353.57 *m/z*) [23,24].

The chromatographic profiles of both extracts (Fig. 1) demonstrated distinct patterns reflecting their different polarities. This different efficiency is visualized in the comparative chromatograms (Fig. 1A-D).

To evaluate the therapeutic potential of *C. foliacea* extracts, we conducted a preliminary screening using the human EGI-1 cholangiocarcinoma cell line. Both extracts demonstrated dose-dependent cytotoxicity against EGI-1 cells (Fig. 2).

Particularly, the ethanol extract and the AcOEt extract showed similar potency with IC_{50} values of 7.16 ± 4.31 μg/mL and 8.18 ± 2.76 μg/mL, respectively. These initial results are promising and provide a strong rationale for further investigating the main metabolite, (*S*)-UA, as a potential anti-CC agent.

Based on these findings, we proceeded to investigate whether the observed anti-CC activity could be attributed to (*S*)-UA, the main metabolite identified in our chemical analysis by

in silico predictions of biological targets and evaluation of (*S*)-UA properties

3.2. *In silico identification of usnic acid potential targets and pharmacokinetic properties*

We conducted comprehensive in silico analyses to predict the therapeutic potential of (*S*)-UA. Using the STITCH (Search Tool for Interacting Chemicals) database [25], which contains a comprehensive resource of known interactions of compounds and proteins. Focusing on *Homo sapiens* proteins, we identified potential protein targets with a medium confidence interaction score > 0.4. Network analysis revealed ten primary interactors (Fig. 3 A), which were further analyzed for their inter-protein interaction (Fig. 3B).

CytoHubba Plugin of Cytoscape [26,27] is an open-source software platform useful for visualizing complex networks and integrating them with any type of attribute data from various databases. It allowed to rank the interactions previously identified by importance, revealing CASP3 and MAPK3 as primary nodes (rank 1), followed by RPS6KBP1 (rank 3), MAPK1 (rank 4), SQSTM1 (rank 5), EIF4EBP1 (rank 6), CASP7 (rank7), XBP1 (rank 8), CASP4 (rank 9) and PDK1 (rank 10). Gene-cancer association enrichment analysis (NDEX-Network Data Exchange, a free Cytoscape Plugin used to search genes between commonly known networks or users uploaded networks) highlighted two particularly relevant targets: MAPK1 and EIF4EBP1. More in detail, MAPK1 is dysregulated in CC, and it is directly involved in the development of head and neck squamous cell carcinoma and non-small cell lung carcinoma. It is also present in a mutated form in tumors as lung adenocarcinoma, colon adenocarcinoma, bladder urothelial carcinoma, endometrial adenocarcinoma, and breast invasive ductal carcinoma [28–30]. EIF4EBP1 is also directly involved in the development of colorectal cancer and gastric adenocarcinoma, and it is overexpressed in some malignant tumors such as breast cancer, gliomas, and glioblastoma.

Drug likeness analysis performed using SwissADME predicted favorable pharmacokinetic properties for (*S*)-UA, including high GI absorption, no predicted P-gp substrate, lead-like properties, and solubility suitable for biological assays.

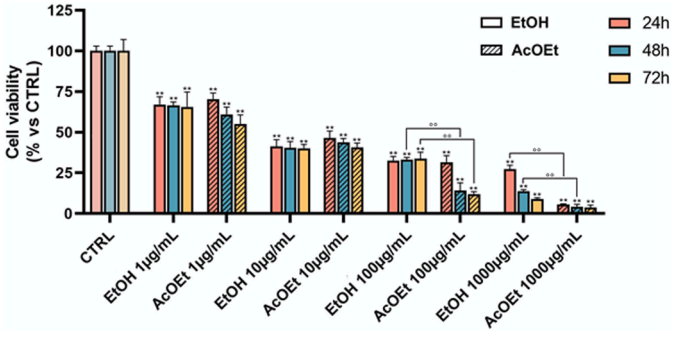

Fig. 2. Cell viability of EGI-1 cell line after the treatment with *C. foliacea* ethanolic extract and AcOEt extracts. Graphs represent the mean percentage ± SD of cell viability compared to untreated controls (CTRL), arbitrarily set to 100 %. ** $p < 0.01$ vs CTRL; °° $p < 0.01$ AcOEt vs EtOH. ** $p < 0.01$ vs CTRL; °° $p < 0.01$ AcOEt vs EtOH.

3.3. *In vitro evaluation of usnic acid antiproliferative potential*

Based on these promising predictions, we optimized a sustainable isolation procedure for (*S*)-UA. Briefly, the ethanolic crude extract was suspended in methanol, centrifuged, and the solid was crystallized from a mixture of chloroform and ethanol, (1/2 v/v), obtaining yellow-orange UA crystals. The chemical structure of (*S*)-UA was confirmed by NMR and MS analysis. The final UA yield has been 0.74 % (expressed as mg of pure metabolite per 100 mg of dry biomass) with a purity > 99 %. The value of the specific optical rotation ($[\alpha]_D^{25} = -476°$) confirmed that the enantiomer present in *C. foliacea* is (—)-(*S*)-UA. The whole process, which avoids chromatographic separations, is associated with a minimum of waste and solvent.

We evaluated both (*S*)-UA and (*R*)-UA effects against human EGI-1 cells to investigate potential enantiospecific differences. The investigation was extended to (*R*) enantiomer, since it is the most diffused in nature and it is easily available in all the most diffused chemical suppliers.

Results obtained demonstrated that (*S*)-UA and (*R*)-UA inhibit EGI-1 cell proliferation in the micromolar range, even if with variable effectiveness (Fig. 4). As evidenced by the graphs and IC_{50} values, both enantiomers generated a significant dose- and time-dependent effect.

Although (S)-UA is twice more active at 24 h, the enantio-preference was shifted at 48 and 72 h, when (*R*)-UA is almost ten times more active than the enantiomer (*S*)-UA, with the most significant differences at low concentrations (2.9 and 29 μM).

To investigate the molecular mechanism involved in the effect of (*R*) and (*S*) UA on EGI-1 CC line, we analyzed in vitro the involvement of MAPK cascade predicted by in silico studies. Human CC EGI-1 cells were treated with both (*S*)-UA and (*R*)-UA, at concentrations below IC_{50} to better investigate their mechanism of action (2.9 and 29 μM). Total protein extracts were performed 30 min, 1, 4, 24, and 48 h after treatment, and results compared to untreated cells considered as control. Phosphorylation and total protein levels of ERK1 (MAPK3) and ERK2 (MAPK1) were evaluated by western blotting experiments (Fig. 5).

In EGI-1 cells treated with (*S*)-UA at 2.9 μM, a significant increase in ERK1 phosphorylation was observed within the first 4 hours compared to untreated controls. For (*S*)-UA 29 μM ERK1 presents a peak of phosphorylation after 1 h, returning comparable to EGI-1 control cells after 24 h (Fig. 5A). Compared to control cells, both 2.9 and 29 μM (*S*)-UA treatment led to an increase in ERK2 phosphorylation at 30 min, followed by a decrease at 1 h, and a subsequent increase at 4 h. At 24 and 48 h, both concentrations of (*S*)-UA resulted in reduction of ERK2 phosphorylation leading to a level lower than control cells (Fig. 5B).

The effect on ERK1 phosphorylation was comparable for 2.9 μM and 29 μM of (*R*)-UA concentrations at all evaluated time points, except at 30 minutes. At this early time point, only 29 μM (*R*)-UA induced a significant increase in ERK1 phosphorylation, while for 2.9 μM (*R*)-UA ERK1 phosphorylation is the same as the control. Subsequent time

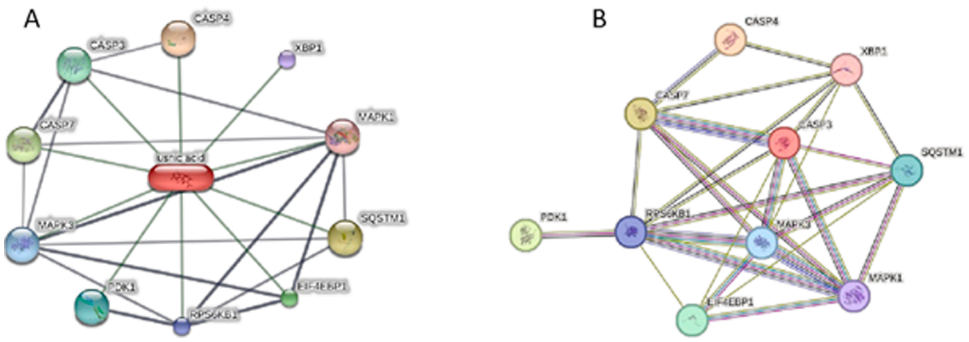

Fig. 3. protein-chemical entity interaction network created with STITCH (A) and PPI network (B).

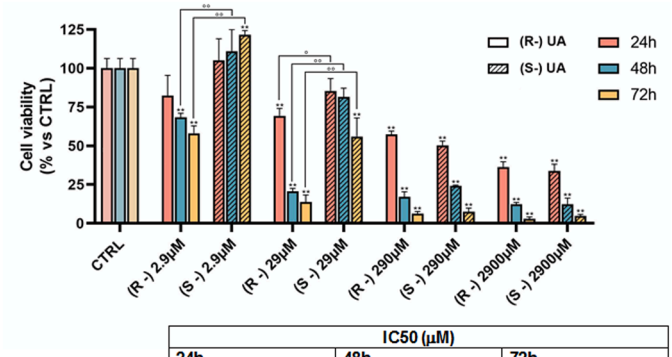

	IC50 (µM)		
	24h	**48h**	**72h**
(*S*)-Usnic acid	377.6 ± 44.2	98.8 ± 9.1	40.7 ± 7.3
(*R*)-Usnic acid	627.43 ± 108.41	4.91±3.2	3.80±1.6

Fig. 4. Cell viability of EGI-1 cells treated with (*S*)-UA and (*R*)-UA. Cells were treated with increasing concentrations of UA enantiomers. After 24, 48 and 72 h MTT assay were performed in triplicate. Graphs represent the mean percentage ± SD of cell viability compared to untreated controls (CTRL), arbitrarily set to 100 %. ** $p < 0.01$ vs CTRL; ° $p < 0.05$ R vs S; °° $p < 0.01$ R vs S.

points up to 4 hours, showed an increased ERK1 phosphorylation compared to the control, returning to control levels at 24 h for both concentrations (Fig. 5C).

Regarding ERK2, (*R*)-UA treatment resulted in a significant increase of ERK2 phosphorylation from 30 minutes to 4 hours for both concentrations, compared to the control. At 24 hours, phosphorylation levels were comparable to the control, but at 48 hours, a slight yet significant reduction in phosphorylation was observed (Fig. 5D).

For all treatments and time points evaluated, total ERK1 and ERK2 levels did not vary significantly compared to controls (data not shown).

Due to the singular effect on the ERK1/2 phosphorylation levels of both the UA enantiomers, we further investigated their mechanism of action. Particularly, we evaluated their direct interaction of enantiomers with the kinases considered so far, exploiting Eurofins Discovery platforms.

Results highlighted that either of the metabolites were able to modulate the ERK1 and ERK2 at any of the tested concentrations (from 0.003 to 30 µM). Consistently, we investigated other UA potential targets applying SAFAN-ISP, S.A.F.AN. BIOINFORMATICS profiling technology. SAFAN-ISP implements a ligand-based approach, evaluating the molecular similarity between the submitted molecule(s) and those included in a refactored bioactivity database derived from CHEMBL31. To sample the chemical space more effectively, similarities are also evaluated on fragments (molecules of low complexity) and combined with whole molecules matches and with a proprietary weighting function between the two. This allows SAFAN-ISP to concurrently predict a compound's ability to interact with 4500 protein targets belonging to 15 different classes, yielding a binding constant as output.

This analysis allowed the identification of a new potential target of UA, namely mitogen-activated protein kinase 2 (MNK2), an enzyme involved in the MAP kinases cascade [31]. The MNK system is upregulated in different tumors [32]. Also in this case, we tested the predicted data thanks to Eurofins Discover, confirming that both the enantiomers were able to bind MNK2 as predicted by SAFAN-ISP, with a slight enantiopreference for (*S*)-UA (IC_{50}= 7.4 µM). Of note, UA has never been associated with MNK2 inhibition, and the direct interaction could explain the ability of this metabolite to modulate the MAP kinases cascade.

3.4. Drug testing on iCCA organoids

The effect of UA enantiomers was also evaluated by using 3D models of cholangiocarcinoma.

Using organoids from two different iCCA patients, we established an appropriate three-dimensional system to test the efficacy of (*S*)-UA and (*R*)-UA treatment.

Following the development of organoid-like structures, we tracked their growth over time with brightfield microscopy, showing how organoids morphologically displayed a cystic form, with an exterior layer defining an interior core (Fig. 6A), as previously mentioned in the literature. In addition, we detected the expression of common biliary markers in iCCA-derived organoids, cytokeratin 7 (CK7) and Epithelial Cell Adhesion Molecule (EpCaM), by using immunofluorescence staining (Fig. 6A).

We evaluated the impact of two different dosages (4 µM and 40 µM) of both (*S*)-UA and (*R*)-UA and monitored cell viability after 72 h with an ATP-based assay. Concentrations were selected based on 2D results obtained at the same time point. For both enantiomers, we observed about a 20 % decrease at 4 µM, while a strong decrease (90 %) at 40 µM dosage was reported. This has also been confirmed morphologically, as at the higher dosage, we observed an altered shape of iCCA organoids (Fig. 6B-C).

In support of these findings, we use the ReViSP algorithm to reconstruct organoid volume trajectories at key time points: 0, 24, 40, 50, 66 and 72 hours after treatment initiation. At 4 µM, a gradual volume decline correlated with a 20 % decrease in viability, while at 40 µM, a swift reduction mirrored a 90 % drop. Volume monitoring indicated more pronounced inhibition than the ATP-based assay for both concentrations (Fig. 6 panel D-E). The temporal alignment of volume dynamics with viability trends fortifies our conclusions, providing a detailed insight into the dose-dependent impact on both cell viability and organoid structure throughout the experimental period.

When considered collectively, our findings showed that organoids produced from iCCA biopsies can serve as a reliable model that enables us to understand the effectiveness and impact of different drugs.

4. Discussion

Cholangiocarcinoma (CC) remains one of the most challenging

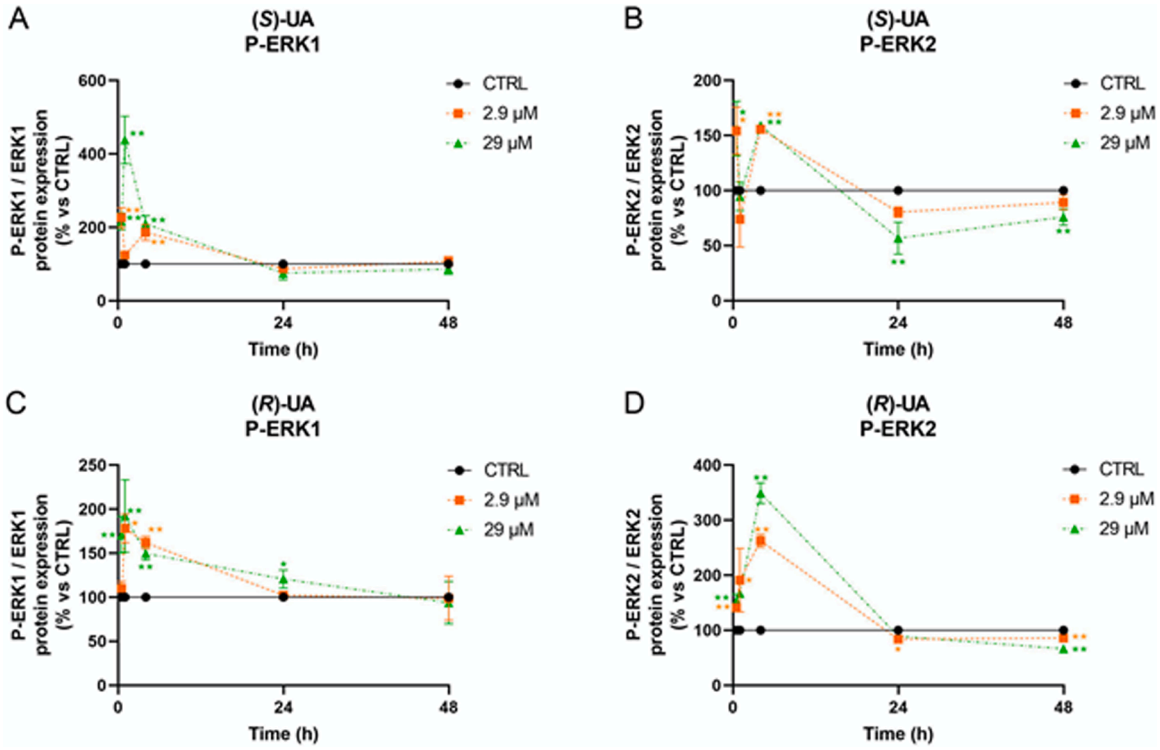

Fig. 5. ERK1 and ERK2 phosphorylation levels after (*S*)-UA and (*R*)-UA treatment. (A) Graph represents the phosphorylation levels of ERK1 after treatment with different concentrations of (S)-UA (2.9 and 29 µM) and at different time points (30 minutes, 1, 4, 24 and 48 hours). (B) Graph represents the phosphorylation levels of ERK2 after treatment with different concentrations of (S)-UA (2.9 and 29 µM) and at different time points (30 minutes, 1, 4, 24 and 48 hours). (C) Graph represents the phosphorylation levels of ERK1 after treatment with different concentrations of (R)-UA (2.9 and 29 µM) and at different time points (30 min, 1, 4, 24 and 48 h). (D) Graph represents the phosphorylation levels of ERK2 after treatment with different concentrations of (R)-UA (2.9 and 29 µM) and at different time points (30 minutes, 1, 4, 24 and 48 hours). Graphs are represented as mean percentage ± SD compared to untreated controls (CTRL), arbitrarily set to 100 %. ** $p < 0.01$, * $p < 0.05$.

biliary tract malignancies, characterized by its aggressive nature, limited therapeutic options, and poor prognosis. In this study, we identified usnic acid (UA) enantiomers as novel anti-CC agents with significant anti-proliferative activity and elucidated their molecular mechanism of action. Our investigation began with isolating (*S*)-UA as the most abundant metabolite from the lichen *Cladonia foliacea*. We subsequently extended our analysis to include (*R*)-UA, the enantiomer most widespread in nature and readily available from commercial suppliers, to comprehensively evaluate potential enantiospecific differences in anti-CC activity. This comparative approach provides valuable insights into structure-activity relationships that could guide future drug development efforts. Both enantiomers demonstrated significant dose- and time-dependent inhibition of EGI-1 cell proliferation in the micromolar range, with notable differences in their efficacy profiles. Interestingly, we observed a time-dependent shift in enantioselectivity. (*S*)-UA exhibited approximately twice the potency of (*R*)-UA at 24 hours, but this preference reversed dramatically at 48 and 72 hours, with (*R*)-UA demonstrating nearly ten-fold greater activity than (*S*)-UA, particularly at lower concentrations (2.9 and 29 µM). This temporal variation in enantioselectivity suggests distinct pharmacodynamic profiles that may involve different cellular uptake rates, metabolism, or engagement with molecular targets. The results obtained herein are particularly interesting if compared with IC_{50} of reference drugs. Thus, in a previous work, we analysed the effect of gemcitabine (GEM) and 5-fluorouracil (5FU) on EGI-1 cell line, and results were in line with UA enantiomers IC_{50} ($GEM_{24\,h}$ >300 µM, $GEM_{48\,h}$= 3 µM, $GEM_{72\,h}$= 0.69 µM; $5FU_{24\,h}$= 76.24 µM, $5FU_{48\,h}$= 2.65 µM, $5FU_{72\,h}$= 0.17 µM) [33].

Our in silico analyses and kinase profiling identified MNK2 as a primary target of UA enantiomers, which we subsequently validated through direct binding and inhibition studies. This finding is particularly significant given the established role of MNK2 in cancer progression through the regulation of protein synthesis via eIF4E phosphorylation. The modulation of this pathway represents a promising therapeutic strategy for CC, a malignancy with limited effective treatment options.

To further explore the molecular mechanisms underlying the anti-proliferative effects of UA enantiomers, we investigated their impact on the MAPK signalling cascade, a pathway implicated in our in silico predictions. Both enantiomers demonstrated complex, time-dependent effects on ERK1/2 phosphorylation, suggesting a sophisticated modulation of MAPK signalling rather than simple inhibition. For (*S*)-UA, we observed a biphasic effect on ERK1 phosphorylation, with significant increases within the first 4 hours followed by a return to baseline levels at 24 hours. Similarly, (*S*)-UA initially enhanced ERK2 phosphorylation at 30 minutes, followed by fluctuations at 1 and 4 hours, and ultimately reduced phosphorylation levels at 24 and 48 hours to below control values. This pattern suggests an initial activation followed by a delayed downregulation of ERK2 signalling. (*R*)-UA displayed distinct effects on MAPK pathway components. Both concentrations tested (2.9 and 29 µM) produced comparable increases in ERK1 phosphorylation from 30 minutes to 4 hours, with a return to control levels at 24 hours. For ERK2, (*R*)-UA induced sustained phosphorylation from 30 minutes to 4 hours, followed by normalization at 24 hours and a slight reduction at 48 hours. These results reveal important enantiospecific differences in MAPK pathway modulation that may contribute to the observed differences in anti-proliferative potency. The downstream consequences of this MAPK pathway modulation were evident in the decreased phosphorylation of eIF4E and subsequent suppression of cancer-promoting proteins. These findings align with the established role of MNK2 as a key regulator of eIF4E activity and protein synthesis, supporting our proposed mechanism of action for UA enantiomers. Perhaps most

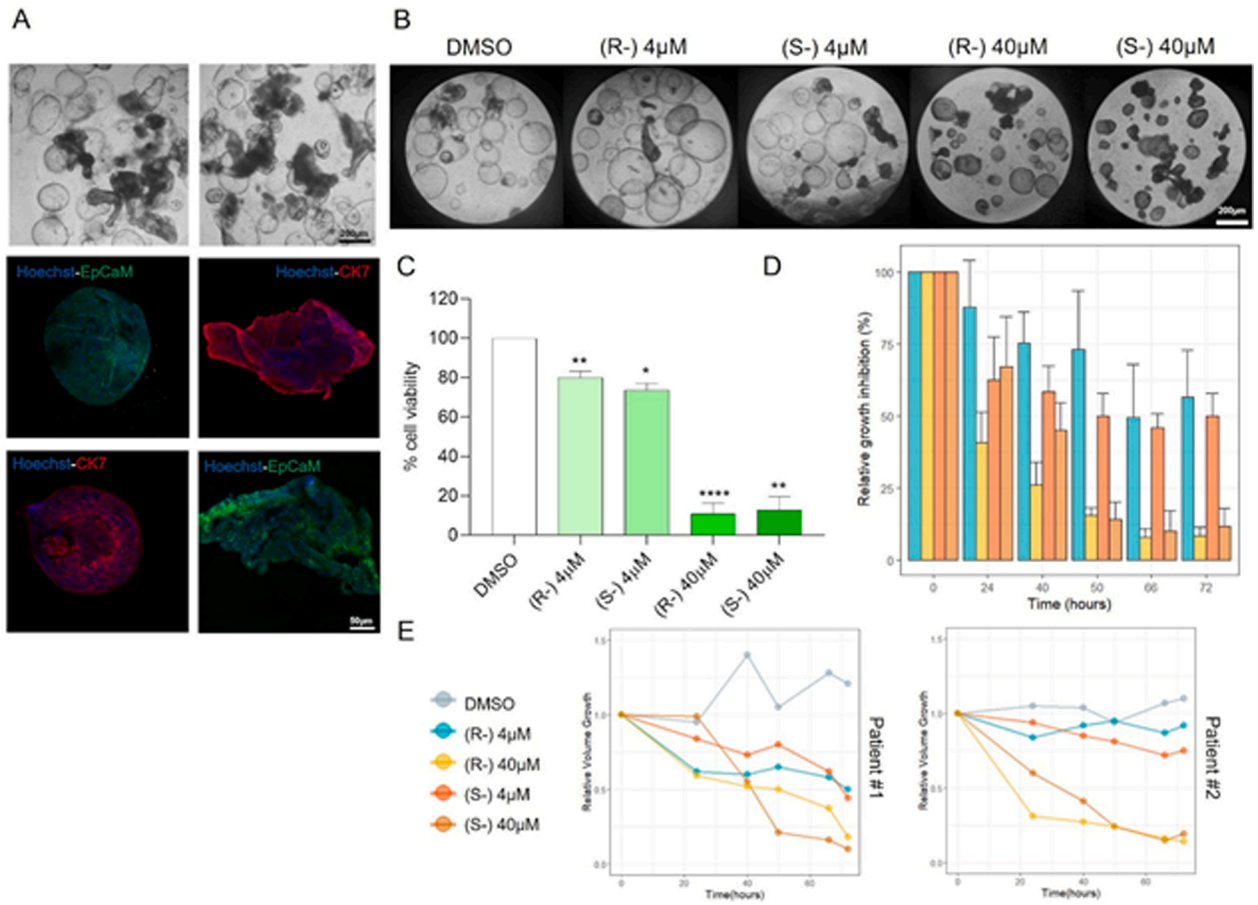

Fig. 6. (A) Representative bright-field images of iCCA patient-derived organoids. Scale bar: 200 μm. Immunofluorescence analysis for iCCA markers EpCaM (green), and CK7 (red) in confocal microscopy. Nuclei were counterstained with Hoechst33342 (blue). Scale bar: 50 μm. (B) Representative bright-field images of tumour organoids exposed to molecules at the indicated concentration for 72 h. DMSO-treated organoids were used as control. Scale bar: 200 μm. (C) The effect of molecules on the viability of iCCA organoids. Viability was measured by the luciferase assay after 72 h exposure to the indicated concentration (*$p < 0005$, **$p < 0.01$, ****$p < 0.001$). DMSO-treated organoids were used as control. (D) The median and standard deviation of relative growth inhibition at different time points. The color legend is shared with Panel E. (E) Relative growth inhibition dynamics over time, stratified by patient, for the different compounds. All experiments were performed at least three independent times and results are shown as mean ± SEM, and an unpaired t test with Welch's correction was applied.

significantly, our studies in patient-derived CC organoids demonstrated that UA treatment resulted in substantial growth inhibition. This finding in advanced 3D models that more accurately recapitulate tumour heterogeneity and microenvironment strengthens the translational potential of our discoveries. The efficacy observed in these organoid models suggests that UA enantiomers may overcome some of the limitations associated with conventional cell culture systems and provides a stronger rationale for further preclinical development. The enantiospecific differences observed in our study highlight the importance of stereochemistry in drug development. The superior long-term efficacy of (*R*)-UA may offer advantages for therapeutic applications, particularly for sustained treatment regimens. However, the more immediate potency of (*S*)-UA could be beneficial in combination therapies or specific treatment contexts. Further investigation into the pharmacokinetic properties and in vivo efficacy of both enantiomers is warranted to fully evaluate their clinical potential. While our findings establish UA as a promising natural product scaffold for CC treatment, several important considerations remain for future studies. First, comprehensive toxicity profiling is needed to assess the safety margin of UA enantiomers, particularly given the known hepatotoxicity associated with some lichen metabolites. However, optimism comes from data obtained in parallel studies on Normal Human Dermal Fibroblasts, which highlight how the IC_{50} values of UA enantiomers are above the toxic dose on this cell line (data not shown). Second, the exploration of potential synergies with existing chemotherapeutic agents could reveal opportunities for combination therapies. Finally, structural optimization of the UA scaffold guided by our mechanistic insights could yield derivatives with enhanced potency, selectivity, and pharmacokinetic properties. In conclusion, our findings establish UA enantiomers as promising candidates for CC treatment through MNK2 targeting and MAPK pathway modulation. The temporal shift in enantioselectivity and distinct effects on MAPK signalling components provide valuable insights into structure-activity relationships that can guide future drug development efforts. As novel therapeutic options for CC remain an urgent unmet clinical need, the natural product scaffold identified in this study represents a significant step forward in addressing this challenging malignancy.

5. Conclusions

In this work, we successfully develop a sustainable protocol to isolate (*S*)-UA from *Cladonia foliacea,* and we perform a first comprehensive comparison of anti-CC activity of UA enantiomers. Furthermore, we identified a novel molecular target (MNK2) and validated the therapeutic potential in advanced 3D models.

The successful translation of activity from 2D to 3D models significantly strengthens the potential of both UA enantiomers as CC therapeutic agents. Morphological changes, such as cellular shrinkage and loss of structural integrity, were also observed, further supporting the cytotoxic effects of the compounds.

Our findings establish UA as a promising natural product scaffold for developing effective cholangiocarcinoma treatments. The direct binding and inhibition of MNK2 represents a novel mechanism of action that warrants further exploration. Future investigations of lichen-derived compounds should carefully consider stereochemical aspects and implement rigorous efficacy assessments before advancing to more complex model systems. Additionally, further preclinical studies are needed to optimize dosing, evaluate potential toxicity, and explore combination therapies that could enhance the therapeutic efficacy of UA enantiomers in cholangiocarcinoma treatment.

CRediT authorship contribution statement

Alessio Malacrida: Writing – original draft, Methodology. **Valeria Cavalloro:** Writing – original draft, Methodology, Formal analysis. **Luisa Pugliese:** Writing – original draft, Software. **Mariarosaria Miloso:** Writing – review & editing. **Emanuela Martino:** Writing – review & editing, Supervision, Conceptualization. **Cristian Turato:** Writing – review & editing, Supervision. **Umberto Mondelli Mario:** Writing – review & editing. **Barbara Oliviero:** Writing – original draft, Methodology. **Stefania Mantovani:** Writing – original draft, Methodology. **Silvia De Siervi:** Writing – original draft, Methodology. **Gabriele Gheza:** Writing – review & editing, Methodology. **Alice Fossati:** Writing – original draft, Methodology. **Alessio Porta:** Writing – review & editing. **Davide Ronchi:** Writing – original draft, Methodology. **Simona Collina:** Writing – review & editing, Supervision, Conceptualization.

Funding

Project funded under the National Recovery and Resilience Plan (NRRP), Mission 4. Component 2 Investment 1.4—Call for tender No. 3138 of 16 December 2021, rectified by Decree n.3175 of 18 December 2021 of Italian Ministry of University and Research funded by the European Union—NextGenerationEU; Award Number: Project code CN_00000033, Concession Decree No. 1034 of 17 June 2022. Adopted by the Italian Ministry of University and Research, CUP, F13C22000720007 Project title "National Biodiversity Future Center—NBFC"

Declaration of Competing Interest

The authors declare that they have no known competing financial interests or personal relationships that could have appeared to influence the work reported in this paper.

Acknowledgements

The authors acknowledge Dr. Teresa Recca and the Centro Grandi Strumenti (CGS) of the University of Pavia for the NMR experiments

Appendix A. Supporting information

Supplementary data associated with this article can be found in the online version at doi:10.1016/j.biopha.2025.118208.

References

[1] J. Ferlay, M. Ervik, F. Lam, M. Colombet, L. Mery, M. Piñeros, E. Al, Global Cancer Observatory: Cancer Today, International Agency for Research on Cancer, Lyon, 2021.

[2] J.M. Banales, V. Cardinale, G. Carpino, M. Marzioni, J.B. Andersen, P. Invernizzi, G.E. Lind, T. Folseraas, S.J. Forbes, L. Fouassier, A. Geier, D.F. Calvisi, J.C. Mertens, M. Trauner, A. Benedetti, L. Maroni, J. Vaquero, R.I.R. Macias, C. Raggi, M. J. Perugorria, E. Gaudio, K.M. Boberg, J.J.G. Marin, D. Alvaro, Cholangiocarcinoma: current knowledge and future perspectives consensus statement from the European Network for the Study of Cholangiocarcinoma (ENS-CCA), Nat. Rev. Gastroenterol. Hepatol. 13 (2016) 261–280, https://doi.org/10.1038/nrgastro.2016.51.

[3] J.W. Valle, R.K. Kelley, B. Nervi, D.-Y. Oh, A.X. Zhu, Biliary tract cancer, Lancet 397 (2021) 428–444, https://doi.org/10.1016/S0140-6736(21)00153-7.

[4] F. Turati, P. Bertuccio, E. Negri, C. La Vecchia, Epidemiology of cholangiocarcinoma, Hepatoma Res. 8 (2022) 19, https://doi.org/10.20517/2394-5079.2021.130.

[5] M. Kuwatani, N. Sakamoto, Promising highly targeted therapies for cholangiocarcinoma: a review and future perspectives, Cancers (Basel) 15 (2023) 3686, https://doi.org/10.3390/cancers15143686.

[6] H. Khizar, Y. Hu, Y. Wu, J. Yang, The role and implication of autophagy in cholangiocarcinoma, Cell Death Discov. 9 (2023) 332, https://doi.org/10.1038/s41420-023-01631-7.

[7] M. Scimeca, V. Rovella, V. Palumbo, M.P. Scioli, R. Bonfiglio, G. Melino, M. Piacentini, L. Frati, M. Agostini, E. Candi, A. Mauriello, Programmed cell death pathways in cholangiocarcinoma: opportunities for targeted therapy, Cancers (Basel) 15 (2023) 3638, https://doi.org/10.3390/cancers15143638.

[8] T. Sato, R.G. Vries, H.J. Snippert, M. van de Wetering, N. Barker, D.E. Stange, J. H. van Es, A. Abo, P. Kujala, P.J. Peters, H. Clevers, Single Lgr5 stem cells build crypt-villus structures in vitro without a mesenchymal niche, Nature 459 (2009) 262–265, https://doi.org/10.1038/nature07935.

[9] H.S. Lee, D.H. Han, K. Cho, S.B. Park, C. Kim, G. Leem, D.E. Jung, S.S. Kwon, C. H. Kim, J.H. Jo, H.W. Lee, S.Y. Song, J.Y. Park, Integrative analysis of multiple genomic data from intrahepatic cholangiocarcinoma organoids enables tumor subtyping, Nat. Commun. 14 (2023) 237, https://doi.org/10.1038/s41467-023-35896-4.

[10] G.S. van Tienderen, M.E.A. van Beek, I.J. Schurink, O. Rosmark, H.P. Roest, J. Tieleman, J. Demmers, I. Muntz, J. Conboy, G. Westergren-Thorsson, G. Koenderink, L.J. van der Laan, M.M.A. Verstegen, Modelling metastatic colonization of cholangiocarcinoma organoids in decellularized lung and lymph nodes, Front. Oncol. 12 (2023), https://doi.org/10.3389/fonc.2022.1101901.

[11] F. Schaub, U. Kim, C. Grandori, A. Zarrinpar, Tumor-derived organoid culture for functional personalized oncology in cholangiocarcinoma, HPB 22 (2020) S26–S27, https://doi.org/10.1016/j.hpb.2020.04.826.

[12] K. Na-Bangchang, T. Plengsuriyakarn, J. Karbwang, The role of herbal medicine in cholangiocarcinoma control: a systematic review, Planta Med 89 (2023) 3–18, https://doi.org/10.1055/a-1676-9678.

[13] D.L. Hawksworth, M. Grube, Lichens redefined as complex ecosystems, N. Phytol. 227 (2020) 1281–1283, https://doi.org/10.1111/nph.16630.

[14] M. Varol, Lichens as a Promising Source of Unique and Functional Small Molecules for Human Health and Well-Being (2019) 425–458, https://doi.org/10.1016/B978-0-444-64181-6.00012-7.

[15] A. Lõhmus, J. Motiejūnaitė, P. Lõhmus, Regionally varying habitat relationships in lichens: the concept and evidence with an emphasis on north-temperate ecosystems, J. Fungi 9 (2023) 341, https://doi.org/10.3390/jof9030341.

[16] A. Galanty, P. Paśko, I. Podolak, Enantioselective activity of usnic acid: a comprehensive review and future perspectives, Phytochem. Rev. 18 (2019) 527–548, https://doi.org/10.1007/s11101-019-09605-3.

[17] M. Xu, E. Oppong-Danquah, X. Wang, S. Oddsson, A. Abdelrahman, S.V. Pedersen, M. Szomek, A.E. Gylfason, B.S. Snorradottir, E.A. Christensen, D. Tasdemir, C. J. Jameson, S. Murad, O.S. Andresson, K.P. Magnusson, H.J. de Boer, M. Thorsteinsdottir, S. Omarsdottir, S. Heidmarsson, E.S. Olafsdottir, Novel methods to characterise spatial distribution and enantiomeric composition of usnic acids in four Icelandic lichens, Phytochemistry 200 (2022) 113210, https://doi.org/10.1016/j.phytochem.2022.113210.

[18] M. Gimła, A. Herman-Antosiewicz, Multifaceted properties of usnic acid in disrupting cancer hallmarks, Biomedicines 12 (2024) 2199, https://doi.org/10.3390/biomedicines12102199.

[19] S. Chen, Z. Ren, L. Guo, Hepatotoxicity of usnic acid and underlying mechanisms, J. Environ. Sci. Heal. Part C 43 (2025) 1–22, https://doi.org/10.1080/26896583.2024.2366737.

[20] H. Wang, M. Xuan, C. Huang, C. Wang, Advances in research on bioactivity, toxicity, metabolism, and pharmacokinetics of usnic acid in vitro and in vivo, Molecules 27 (2022) 7469, https://doi.org/10.3390/molecules27217469.

[21] V. Cavalloro, G. Marrubini, R. Stabile, D. Rossi, P. Linciano, G. Gheza, S. Assini, E. Martino, S. Collina, Microwave-assisted extraction and HPLC-UV-CD determination of (S)-usnic acid in Cladonia foliacea, Molecules 26 (2021) 455, https://doi.org/10.3390/molecules26020455.

[22] E. Farkas, M. Xu, A.M. Muhoro, K. Szabó, A. Lengyel, S. Heiðmarsson, E.Ö. Viktorsson, E.S. Ólafsdóttir, The algal partnership is associated with quantitative variation of lichen specific metabolites in Cladonia foliacea from Central and Southern Europe, Symbiosis 92 (2024) 403–419, https://doi.org/10.1007/s13199-024-00982-8.

[23] R. Brakni, M. Ali Ahmed, P. Burger, A. Schwing, G. Michel, C. Pomares, L. Hasseine, L. Boyer, X. Fernandez, A. Landreau, T. Michel, UHPLC-HRMS/MS based profiling of algerian lichens and their antimicrobial activities, Chem. Biodivers. 15 (2018), https://doi.org/10.1002/cbdv.201800031.

[24] D. Olivier-Jimenez, M. Chollet-Krugler, D. Rondeau, M.A. Beniddir, S. Ferron, T. Delhaye, P.-M. Allard, J.-L. Wolfender, H.J.M. Sipman, R. Lücking, J. Boustie, P. Le Pogam, A database of high-resolution MS/MS spectra for lichen metabolites, Sci. Data 6 (2019) 294, https://doi.org/10.1038/s41597-019-0305-1.

[25] D. Szklarczyk, A. Santos, C. von Mering, L.J. Jensen, P. Bork, M. Kuhn, STITCH 5: augmenting protein–chemical interaction networks with tissue and affinity data, Nucleic Acids Res. 44 (2016) D380–D384, https://doi.org/10.1093/nar/gkv1277.

[26] C.-H. Chin, P.-W. Chen, C.-W. Ho, S.-H. Chen, M.-T. Ko, C.-Y. Lin, cytoHubba (2017).

[27] P. Shannon, A. Markiel, O. Ozier, N. Baliga, J. Wang, D. Ramage, N. Amin, B. Schwikowski, T. Ideker, Cytoscape: a software environment for integrated models of biomolecular interaction networks, Genome Res. 13 (2003) 2498–2504.
[28] M. Burotto, V.L. Chiou, J. Lee, E.C. Kohn, The MAPK pathway across different malignancies: a new perspective, Cancer 120 (2014) 3446–3456, https://doi.org/10.1002/cncr.28864.
[29] H.-L. Ngan, Y. Liu, A.Y. Fong, P.H.Y. Poon, C.K. Yeung, S.S.M. Chan, A. Lau, W. Piao, H. Li, J.S.W. Tse, K.-W. Lo, S.M. Chan, Y.-X. Su, J.Y.K. Chan, C.W. Lau, G. B. Mills, J.R. Grandis, V.W.Y. Lui, MAPK pathway mutations in head and neck cancer affect immune microenvironments and ErbB3 signaling, Life Sci. Alliance 3 (2020) e201900545, https://doi.org/10.26508/lsa.201900545.
[30] R. Caeser, C. Hulton, E. Costa, V. Durani, M. Little, X. Chen, S.E. Tischfield, M. Asher, F.E. Kombak, S.S. Chavan, N.S. Shah, M. Ciampricotti, E. de Stanchina, J. T. Poirier, C.M. Rudin, T. Sen, MAPK pathway activation selectively inhibits ASCL1-driven small cell lung cancer, IScience 24 (2021) 103224, https://doi.org/10.1016/j.isci.2021.103224.
[31] S. Soni, P. Anand, Y.S. Padwad, MAPKAPK2: the master regulator of RNA-binding proteins modulates transcript stability and tumor progression, J. Exp. Clin. Cancer Res. 38 (2019) 121, https://doi.org/10.1186/s13046-019-1115-1.
[32] C. Pinto-Díez, R. Ferreras-Martín, R. Carrión-Marchante, V.M. González, M. E. Martín, Deeping in the Role of the MAP-kinases interacting kinases (MNKs) in cancer, Int. J. Mol. Sci. 21 (2020) 2967, https://doi.org/10.3390/ijms21082967.
[33] A. Malacrida, R. Rigolio, L. Celio, S. Damian, G. Cavaletti, V. Mazzaferro, M. Miloso, In Vitro evaluation of rigosertib antitumoral and radiosensitizing effects against human cholangiocarcinoma cells, Int. J. Mol. Sci. 22 (2021) 8230, https://doi.org/10.3390/ijms22158230.